Effect of tube diameter and capillary number on platelet margination and near-wall dynamics

Rheologica Acta manuscript No.
(will be inserted by the editor)

Effect of tube diameter and capillary number on platelet margination and near-wall dynamics

Timm Krüger

Received: date / Accepted: date

Abstract I investigate the effect of tube diameter D and red blood cell capillary number Ca (i.e. the ratio of viscous to elastic forces) on platelet margination in blood flow at $\approx 37\%$ tube haematocrit. The system is modelled as three-dimensional suspension of deformable red blood cells and nearly rigid platelets using a combination of the lattice-Boltzmann, immersed boundary and finite element methods. Results of simulations during the dynamics before the steady state has been reached show that a non-diffusive radial platelet transport facilitates margination. This non-diffusive effect is important near the edge of the cell-free layer, but only for $Ca > 0.2$, when red blood cells are tank-treading. I also show that platelet trapping in the cell-free layer is reversible for $Ca \leq 0.2$. Margination is essentially independent of Ca only for the smallest investigated tube diameter ($D = 10\,\mu\text{m}$). Once platelets have reached the cell-free layer, they tend to slide rather than tumble. The tumbling rate is essentially independent of Ca but increases with D. Strong confinement suppresses tumbling due to the relatively small cell-free layer thickness at $\approx 37\%$ tube haematocrit.

Keywords Platelet margination · red blood cell · cell-free layer · lattice-Boltzmann method · immersed boundary method · simulation

Special Issue "Rheology of blood cells, capsules and vesicles"

Timm Krüger
University of Edinburgh
School of Engineering
King's Buildings
Mayfield Road
Edinburgh EH9 3FB
Tel.: +44 131-650-5679
Fax: +44 131-650-6554
E-mail: timm.krueger@ed.ac.uk

PACS 47.63.Cb · 47.57.E- · 47.63.mh

Mathematics Subject Classification (2010) 76Z05

1 Introduction

The aim of this article is to investigate the effect of tube diameter and capillary number (wall shear rate) on the margination and near-wall dynamics of platelets in blood flow via highly resolved three-dimensional computer simulations. Platelet adhesion or activation are not in the focus of this research.

Human blood is, by volume, composed of about 55% plasma (mostly water and proteins) and 45% suspended blood cells. The majority of the blood cells are red blood cells (RBCs), also called erythrocytes. Other, less common blood cells are white blood cells (leukocytes, one for 1000 RBCs) which form a significant part of the immune system (Robertson et al, 2007) and platelets (thrombocytes, one for 15 RBCs) (AlMomani et al, 2008). The volume fraction of the cellular phase is called haematocrit Ht.

Platelets play an important role in the process of blood clotting and the repair of damaged vessel walls (endothelium). By mechanical contact with damaged endothelium, platelets can be activated. The activation involves a reorganisation of the platelet cytoskeleton, making them more flexible (Fogelson and Guy, 2008). Activated platelets are capable of forming networks via fibrinogen and von Willebrand factor molecules giving rise to the build-up of blood clots (Kulkarni et al, 2000; Doggett et al, 2002). Non-activated platelets can be considered as rigid discoid particles over the entire physiological shear stress range (up to a few

10 Pa) (Goldsmith and Mason, 1967; Teirlinck et al, 1984; Turitto and Goldsmith, 1992).

The main task of platelets is to recognise regions of damaged endothelium and to assist in its repair. Indeed, the platelet concentration is, under certain conditions, significantly increased close to the walls (Turitto et al, 1972; Goldsmith and Turitto, 1986). This near-wall excess is of physiological importance as it increases the probability for the platelets to adhere to the damaged endothelium (Yeh and Eckstein, 1994). Platelet concentration near the wall can be several times higher than that at the centre of the flow (Tangelder et al, 1982; Tilles and Eckstein, 1987; Aarts et al, 1988; Eckstein et al, 1989). The lateral motion of platelets, leading to this concentration inhomogeneity, is called *margination*. Usually, the near-wall concentration peak is located within or near the cell-free layer (CFL) which is depleted of RBCs (Yeh and Eckstein, 1994). The CFL thickness ℓ_{CFL} plays an important role in blood flow, leading to the Fåhræus and Fåhræus-Lindqvist effects (Fåhræus and Lindqvist, 1931; Lei et al, 2013).

RBCs have a twofold effect on the platelet motion. First, the presence of RBCs increases the diffusivity of platelets in blood vessels by orders of magnitude compared with their Brownian diffusivity (Aarts et al, 1983, 1984; Breugel et al, 1992; Turitto and Goldsmith, 1992). Furthermore, non-diffusive platelet margination towards the vessel wall increases strongly when RBCs are present (Turitto and Weiss, 1980; Cadroy and Hanson, 1990; Joist et al, 1998; Peerschke et al, 2004).

The wall shear stress and the haematocrit are important parameters for margination (Turitto and Baumgartner, 1975, 1979; Turitto and Goldsmith, 1992; Zhao et al, 2007; Fogelson and Guy, 2008; Reasor Jr et al, 2013). It is known that margination is only significant when the wall shear rate is above $200\,\mathrm{s}^{-1}$ (Tilles and Eckstein, 1987; Eckstein et al, 1988; Bilsker et al, 1989). There also seems to be a minimum haematocrit of 10% below which no margination occurs for physiological stresses (Tilles and Eckstein, 1987; Waters and Eckstein, 1990). Margination becomes more important with increasing haematocrit (Yeh and Eckstein, 1994). Also platelet size and shape play a role for the margination efficiency (Eckstein et al, 1988; Thompson et al, 2013; Reasor Jr et al, 2013; Müller et al, 2014).

Only in recent years, resolved computer simulations became available to study the mechanisms of platelet margination directly, without assuming effective platelet transport models. Simulations are able to provide microscopic details (such as stresses, cell velocities and deformations) that are difficult to measure in experiments. As already assumed in the 1970s by Goldsmith (1971) and Turitto et al (1972), it is nowadays generally accepted that the dynamics of RBCs and their hydrodynamic interactions with platelets under the influence of shear are responsible for margination, rather than a volume exclusion effect (Crowl and Fogelson, 2010). Zhao and Shaqfeh (2011) found that the lateral platelet motion in the RBC-rich region is diffusive and caused by shear-induced fluid velocity fluctuations. According to Kumar and Graham (2012b), platelet margination, at least in the dilute regime, is caused by heterogeneous collisions of platelets and RBCs. If the RBCs are sufficiently soft, these collisions lead to directed events which are necessary to explain margination (Eckstein and Belgacem, 1991). It can be concluded that the dynamical state of RBCs (tank-treading versus tumbling or sliding) plays a major role in platelet margination, as already suggested by Yeh and Eckstein (1994). Recent review articles provide more details (Kumar and Graham, 2012a; Fogelson and Neeves, 2015).

In general, platelet margination is still not well understood. This research aims at investigating in more detail the effect of tube diameter and capillary number on margination. Three-dimensional computer simulations employing the lattice-Boltzmann, immersed boundary and finite element methods (section 2) are performed to investigate platelet trajectories in an environment of deformable RBCs. Section 3 presents the relevant parameter space and the system setup. The results about platelet margination and platelet dynamics in the CFL are presented and discussed in section 4. Finally, section 5 contains the conclusions.

2 Physical model and numerical methods

There are several recent publications by different research groups simulating cellular blood flow, e.g. Dupin et al (2007); MacMeccan et al (2009); Doddi and Bagchi (2009); Fedosov et al (2011); Zhao and Shaqfeh (2011); Freund (2014); Fedosov et al (2014a). Details and benchmark tests concerning the present model are reported elsewhere (Krüger, 2011; Krüger et al, 2011, 2013, 2014). The lattice-Boltzmann method (section 2.1) is used as Navier-Stokes solver, and the immersed boundary method (section 2.2) couples the fluid and structure dynamics. For the membranes of the red blood cells, a finite element approach (section 2.3) is employed. Section 2.4 contains an outline of the numerical implementation of the viscosity contrast. Tab. 1 provides an overview of all relevant symbols and parameters.

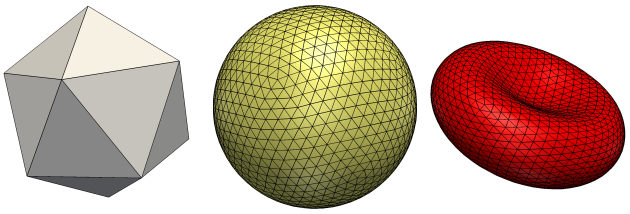

(a) (b) (c)

Fig. 1 Mesh generation for a red blood cell. The 20 face elements of an icosahedron (a) are subdivided, and the resulting new vertices shifted to the circumsphere (b). The mesh of a red blood cell (c) can be obtained by adjusting the vertex positions in space. The meshes in (b) and (c) have 2880 elements each.

Fig. 2 Indicator field $I(\mathbf{x})$ for distinguishing between interior and exterior fluid sites. A two-dimensional cross-section of a three-dimensional RBC suspension in a tube is shown. Red lines denote the Lagrangian membranes. The grey-scale lattice-like portion of the figure reflects $I(\mathbf{x})$ on the same cross-section. Black denotes the interior, white the exterior.

2.1 Lattice-Boltzmann method

The standard lattice-Boltzmann method with D3Q19 lattice (Qian et al, 1992) and BGK collision operator (Bhatnagar et al, 1954) is employed to solve the Navier-Stokes equations (Succi, 2001; Aidun and Clausen, 2010).

The BGK operator is parametrised by a relaxation time $\tau\Delta t$ (with Δt being the time step). The kinematic fluid viscosity is directly related to τ according to

$$\nu = \frac{1}{3}\left(\tau - \frac{1}{2}\right)\frac{\Delta x^2}{\Delta t} \tag{1}$$

where Δx is the lattice resolution.

External forces, such as those from the immersed boundary method (section 2.2), are coupled through the forcing scheme by Shan and Chen (Shan and Chen, 1993).

2.2 Immersed boundary method

The immersed boundary method (IBM) (Peskin, 1972, 2002) couples the fluid flow on the Eulerian lattice and the off-lattice membrane interface dynamics. IBM has often been employed for the simulation of elastic deformable objects, e.g. by Eggleton and Popel (1998); Zhang et al (2007); Sui et al (2008); Fogelson and Guy (2008); Doddi and Bagchi (2009).

Fluid velocities are interpolated at the locations of the membrane vertices, and membrane forces (section 2.3) are distributed back to the lattice. For this purpose, a short-range tri-linear interpolation stencil is used that requires only 2^3 lattice points in three dimensions (Peskin, 2002).

2.3 Red blood cell mesh and elasticity model

In their undeformed state, RBCs are biconcave discs with a diameter of about $8\,\mu$m. RBC membranes are characterised by two major elastic contributions: in-plane shear and bending resistance (Skalak et al, 1973; Evans, 1974). Furthermore, local and global area changes are small (typically below 1%) since the lipid bilayer is incompressible. The total RBC surface $A^{(0)}$ is therefore essentially constant. Under physiological conditions, the RBC volume, $V^{(0)}$, is also constant (Evans and Fung, 1972). The strong deformability of RBCs is facilitated by the large area excess (additional area compared to a sphere with the same volume) which is about 35%. This way, RBCs can squeeze through capillaries with diameters as small as $4\,\mu$m without violating the surface and volume constraints (Skalak and Branemark, 1969).

In the present work, RBCs and platelets are treated as closed membranes discretised by N_f flat faces (area elements). Each element consists of three nodes (vertices) of which there are in total $N_\mathrm{n} = (N_\mathrm{f} + 4)/2$. The generation of the RBC mesh, depicted in Fig. 1, is based on the icosahedron-refinement procedure (Ramanujan and Pozrikidis, 1998; Krüger, 2011). In the present work, each RBC mesh consists of 2880 elements and 1442 vertices. Platelets are assumed to be non-activated and modelled as nearly rigid (i.e. with finite but large elastic moduli and negligible deformations for the current purpose), oblate ellipsoids with an aspect ratio 0.28 and major radius of $1.8\,\mu$m. Each platelet mesh comprises 320 faces and 162 vertices.

The RBC membrane is modelled as a hyperelastic continuum with four elastic energy contributions as outlined below. The model neglects membrane viscosity and assumes that undeformed RBCs are stress-free.

The RBC equilibrium shape is imposed through the input geometry in Fig. 1(c).

Skalak's constitutive law for the in-plane energy density is employed in the present simulations (Skalak et al, 1973):

$$E_{\mathrm{S}} = \int \mathrm{d}A \left(\frac{\kappa_{\mathrm{S}}}{12} \left(I_1^2 + 2I_1 - 2I_2 \right) + \frac{\kappa_\alpha}{12} I_2^2 \right). \tag{2}$$

The two parameters κ_{S} and κ_α control the strength of the membrane response to local shear deformation and dilation, respectively. For healthy RBCs, the values are $\kappa_{\mathrm{S}} = 5.3\,\mu\mathrm{N\,m^{-1}}$ and $\kappa_\alpha = 0.5\,\mathrm{N\,m^{-1}}$ (Gompper and Schick, 2008). The two strain invariants I_1 and I_2 describe the in-plane deformation and represent the local shear deformation and area dilation, respectively. Eq. (2) is discretised on the membrane mesh according to Charrier et al (1989) and Shrivastava and Tang (1993). More details are provided by Krüger et al (2011).

For the bending energy, the ad-hoc form

$$E_{\mathrm{B}} = \frac{\sqrt{3}\kappa_{\mathrm{B}}}{2} \sum_{\langle i,j \rangle} \left(\theta_{ij} - \theta_{ij}^{(0)} \right)^2, \tag{3}$$

similar to that in Fedosov et al (2014b), is used. Here, κ_{B} is the bending resistance ($2 \cdot 10^{-19}\,\mathrm{N\,m}$ for an RBC), θ_{ij} is the angle between the normal vectors $\hat{\mathbf{n}}_i$ and $\hat{\mathbf{n}}_j$ of two neighbouring elements, and $\theta_{ij}^{(0)}$ is the corresponding equilibrium angle of the undeformed membrane. The sum runs over all pairs of neighbouring elements.

In order to maintain a nearly constant RBC surface area and following Evans and Skalak (1980) and Seifert (1997), an additional energy is introduced:

$$E_{\mathrm{A}} = \frac{\kappa_{\mathrm{A}}}{2} \frac{\left(A - A^{(0)} \right)^2}{A^{(0)}}. \tag{4}$$

Here, A and $A^{(0)}$ are the current and reference RBC surface areas. For a healthy RBC one finds $A^{(0)} \approx 140\,\mu\mathrm{m}^2$. While $A^{(0)}$ is used as input parameter, A is computed at every time step by summing all surface element areas. The magnitude of the surface energy is controlled by the surface stretching modulus κ_{A} that reflects the incompressibility of the lipid bilayer. A similar approach is used for the RBC volume (Seifert, 1997):

$$E_{\mathrm{V}} = \frac{\kappa_{\mathrm{V}}}{2} \frac{\left(V - V^{(0)} \right)^2}{V^{(0)}} \tag{5}$$

with V and $V^{(0)} \approx 100\,\mu\mathrm{m}^3$ being the current and reference RBC volumes.

The total membrane energy E is the sum of all contributions E_{S}, E_{B}, E_{A} and E_{V}. The principle of virtual work allows to compute the forces acting on membrane vertices at position $\mathbf{r}_j$ from the energy functional $E(\{\mathbf{r}_j\})$:

$$\mathbf{F}_j = -\frac{\partial E(\{\mathbf{r}_j\})}{\partial \mathbf{r}_j}. \tag{6}$$

The differentiation is performed analytically, and the resulting forces are implemented in the code. A detailed derivation of all force contributions is given by Krüger (2011).

To avoid particle overlap during the simulation, a short-range repulsion force acts between pairs of neighbouring mesh nodes that belong to different RBCs or platelets. This force is the same as in Gross et al (2014); it vanishes for distances larger than Δx and increases for smaller node-node distances. A test simulation with higher resolution ($r_{\mathrm{RBC}} = 16\Delta x$ rather than $12\Delta x$) gave the same radial haematocrit distribution. Therefore, the repulsion force does not seem to play an important role at the chosen resolution and haematocrit value.

2.4 Viscosity contrast

In order to implement a viscosity contrast Λ, i.e. different viscosities inside and outside of the RBCs, each lattice site requires up-to-date information about its location relative to nearby Lagrangian vertices. A signed distance field as detailed by Frijters et al (2015) is used to construct an indicator field $I(\mathbf{x})$ at each lattice site $\mathbf{x}$, denoting the relative location of each site with respect to nearby RBCs and platelets ($I = 0$ outside and $I = 1$ inside particles with a linear slope across the particle surface). The instantaneous kinematic viscosity is then

$$\nu(\mathbf{x}) = \nu_{\mathrm{out}} \left(1 - I(\mathbf{x}) \right) + \nu_{\mathrm{in}} I(\mathbf{x}) \tag{7}$$

where ν_{out} and ν_{in} are the external and internal viscosities, respectively, and

$$\Lambda = \frac{\nu_{\mathrm{in}}}{\nu_{\mathrm{out}}} \tag{8}$$

is the viscosity contrast. Fig. 2 shows the indicator field for a given RBC configuration.

3 System parameters and simulation setup

After introducing the relevant system parameters in section 3.1, the choice of simulation parameters is briefly described in section 3.2. The initialisation of the simulations (section 3.3) deserves some additional attention.

3.1 Physical parameters

The present research concerns with blood flow in straight tubes, which involves a series of parameters and related symbols as collected in Tab. 1.

A pressure gradient p', mimicked by a constant and homogeneous force density $f = p'$, drives the flow along the tube axis in positive x-direction. In the absence of particles, this would lead to a parabolic velocity profile with peak velocity $\hat{u}_0 = p'D^2/(16\eta_{\mathrm{ex}})$, average velocity $\bar{u}_0 = \hat{u}_0/2$ and wall shear rate $\dot{\gamma}_{\mathrm{w}} = 4\hat{u}_0/D$.

The deformation of an RBC with radius r_{RBC} and shear elasticity κ_{S} in a simple viscous shear flow with viscosity η and shear rate $\dot{\gamma}$ is characterised by the capillary number $Ca = \eta\dot{\gamma}r_{\mathrm{RBC}}/\kappa_{\mathrm{S}}$. In a Poiseuille flow, the shear rate is not constant, but it is common to denote the shear rate magnitude by the wall shear rate $\dot{\gamma}_{\mathrm{w}}$. Accordingly, the "wall capillary number" in tube flow is defined by

$$Ca = \frac{\eta_{\mathrm{ex}}\dot{\gamma}_{\mathrm{w}}r_{\mathrm{RBC}}}{\kappa_{\mathrm{S}}} = \frac{p'Dr_{\mathrm{RBC}}}{4\kappa_{\mathrm{S}}}. \tag{9}$$

The second equality can be confirmed by replacing $\dot{\gamma}_{\mathrm{w}}$ and $\hat{u}_0$ by the expressions given above. Note that no RBC in the tube is actually experiencing the wall shear rate because all RBCs are located farther inside where the shear rates are lower. However, $\dot{\gamma}_{\mathrm{w}}$ is still a good indicator of the typical shear rates close to the vessel wall.

Table 1 Overview of used parameters and symbols.

Parameter	symbol	value
Tube radius, diameter	R, D	variable
Tube segment length	L	$48\,\mu\mathrm{m}$
RBC radius	r_{RBC}	$4\,\mu\mathrm{m}$
Platelet radius	r_{pl}	$1.8\,\mu\mathrm{m}$
Platelet thickness	h_{pl}	$1\,\mu\mathrm{m}$
Tube haematocrit	Ht_{t}	$\approx 37\%$
RBC count	N_{RBC}	variable
Platelet count	N_{pl}	$N_{\mathrm{pl}} = N_{\mathrm{RBC}}/2$
Fluid density	ρ	$1000\,\mathrm{kg\,m^{-3}}$
Cytoplasm viscosity	η_{in}	$5\,\mathrm{mPa\,s}$
Plasma viscosity	η_{ex}	$1\,\mathrm{mPa\,s}$
viscosity contrast	Λ	5
RBC shear elasticity	κ_{S}	$5.3\,\mu\mathrm{N\,m^{-1}}$
RBC bending rigidity	κ_{B}	$2\cdot10^{-19}\,\mathrm{N\,m}$
Reduced bending modulus	$\kappa_{\mathrm{B}}/(\kappa_{\mathrm{S}}r^2)$	1/424
Pressure gradient	p'	variable
Capillary number	Ca	variable
Lattice resolution	Δx	$0.33\,\mu\mathrm{m}$
Time step	Δt	variable
Centre velocity (no cells)	$\hat{u}_0$	$0.05\,\Delta x/\Delta t$
Average velocity (no cells)	$\bar{u}_0$	$\hat{u}_0/2$
Wall shear rate	$\dot{\gamma}_{\mathrm{w}}$	$4\hat{u}_0/D$
Number of time steps	N_t	$2\cdot10^5$
Advection time	t_{ad}	$960\,\Delta t$

Under physiological conditions (η_{ex}, κ_{S} and r_{RBC} as reported in Tab. 1), $Ca = 1$ corresponds to $\dot{\gamma}_{\mathrm{w}} \approx 1300\,\mathrm{s^{-1}}$, which leads to significant RBC deformations. Note that the definition of Ca in Poiseuille flow is not unique and that there may be a constant conversion factor between the present and other authors' choice.

The purpose of this article is to investigate the effect of tube diameter D and capillary number Ca on the platelet dynamics in tube flow at physiological blood parameters. Tab. 2 lists the investigated values for D and Ca. The tube haematocrit is $Ht_{\mathrm{t}} \approx 37\%$ in all cases.

In order to find a dimensionless time for the *advection* of the suspension, one may define the advection time scale

$$t_{\mathrm{ad}} = \frac{2r_{\mathrm{RBC}}}{\bar{u}_0}. \tag{10}$$

It is the average time an RBC requires to move its own diameter in the unperturbed flow.

3.2 Simulation parameters

The flow is periodic along the tube axis (x-direction). The circular tube cross-section is approximated by a

Table 2 Overview of numerical simulation parameters. [s.u.] denotes "simulation units". Symbols are explained in Tab. 1. Other simulation parameters that are the same throughout are $\nu_{\mathrm{in}} = 5/6$, $\nu_{\mathrm{ext}} = 1/6$, $Ht_{\mathrm{t}} \approx 37\%$, $\kappa_\alpha = 0.5$, $\kappa_{\mathrm{A}} = \kappa_{\mathrm{V}} = 1$ and $N_t = 2\cdot10^5$.

D [μm]	Ca	N_{pl}	p' [s.u.]	κ_{S} [s.u.]	κ_{B} [s.u.]
10	0.1	7	$1.48\cdot10^{-4}$	0.133	0.0453
	0.2			0.0666	0.0226
	0.3			0.0444	0.0151
	0.6			0.0222	0.00755
	1.0			0.00453	0.00453
	2.0			0.00666	0.00226
15	0.1	16	$6.58\cdot10^{-5}$	0.0888	0.0302
	0.2			0.0444	0.0151
	0.3			0.0296	0.0101
	0.6			0.0148	0.00503
	1.0			0.00888	0.00302
	2.0			0.00444	0.00151
20	0.1	28	$3.70\cdot10^{-5}$	0.0666	0.0226
	0.2			0.0333	0.0113
	0.3			0.0222	0.00755
	0.6			0.0111	0.00377
	1.0			0.00666	0.00226
	2.0			0.00333	0.00113
30	0.1	63	$1.65\cdot10^{-5}$	0.0444	0.0151
	0.2			0.0222	0.00755
	0.3			0.0148	0.00503
	0.6			0.00741	0.00252
	1.0			0.00444	0.00151
	2.0			0.00222	0.000755

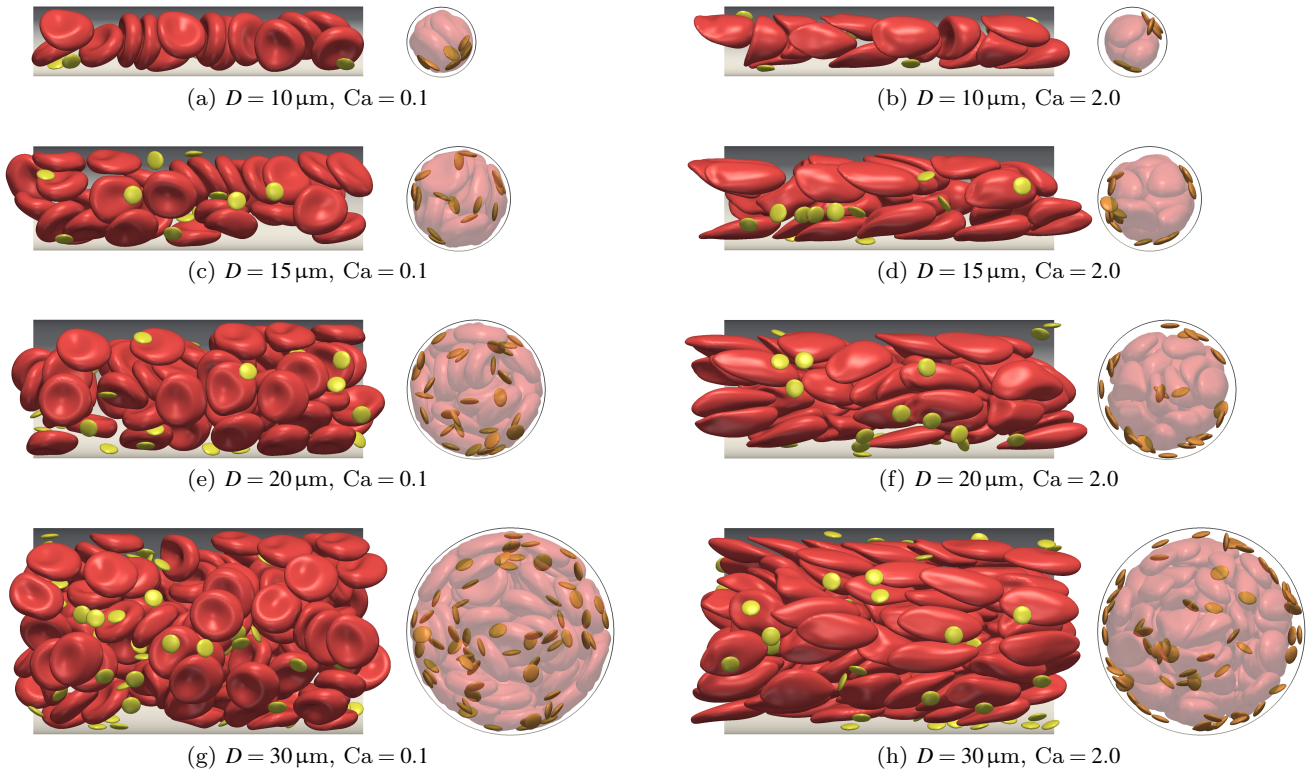

(a) $D = 10\,\mu\text{m}$, $\text{Ca} = 0.1$ (b) $D = 10\,\mu\text{m}$, $\text{Ca} = 2.0$

(c) $D = 15\,\mu\text{m}$, $\text{Ca} = 0.1$ (d) $D = 15\,\mu\text{m}$, $\text{Ca} = 2.0$

(e) $D = 20\,\mu\text{m}$, $\text{Ca} = 0.1$ (f) $D = 20\,\mu\text{m}$, $\text{Ca} = 2.0$

(g) $D = 30\,\mu\text{m}$, $\text{Ca} = 0.1$ (h) $D = 30\,\mu\text{m}$, $\text{Ca} = 2.0$

Fig. 3 Configuration of the red blood cells (red) and platelets (yellow) for all investigated tube diameters ($D = 10$, 15, 20, $30\,\mu\text{m}$) and the smallest and largest studied capillary numbers ($Ca = 0.1$, 2.0) at $Ht_\text{t} \approx 37\%$ after $t = 208 t_\text{ad}$. The left columns show sections along the tube, the right columns tube cross-sections with reduced RBC opacity to reveal all platelets. Flow is from left to right (left columns) and out of the image plane (right columns).

staircase, and the half-way bounce-back boundary condition is used to enfore no-slip at the wall (Ladd, 1994). Due to the large tube diameters and the choice of the external viscosity, artificial numerical slip is negligible.

The lattice resolution is $\Delta x = 0.33\,\mu\text{m}$, *i.e.* the RBC diameter is $2r_\text{RBC} = 8\,\mu\text{m} = 24\Delta x$. While the tube diameter D varies, the length of the simulated tube segment is $L = 12 r_\text{RBC} = 144\Delta x$ in all simulations.

Obeying $\Lambda = 5$, the viscosities are $\nu_\text{ex} = 1/6$ and $\nu_\text{in} = 5/6$ in simulation units. This leads to BGK relaxation parameters $\tau_\text{ex} = 1$ and $\tau_\text{in} = 3$, according to Eq. (1).

The flow is driven by a constant force density $f = p'$ along the tube axis. Its value is chosen in such a way that the centre velocity $\hat{u}_0$ would be $0.05\,\Delta x/\Delta t$ in the absence of any particles. This is to avoid compressibility effects and to keep the time step sufficiently small to achieve stable simulations. Note that the actual centre velocity is smaller (typically by a factor of ≈ 2) due to the presence of the cells.

Tab. 2 lists all relevant parameter values for the simulations undertaken.

3.3 Simulation initialisation

Due to the relatively small system size (between $N_\text{RBC} = 14$ and 126), the number of platelets is $N_\text{pl} = N_\text{RBC}/2$. This is about 7–8 times larger than observed under physiological conditions. Since platelets are much smaller than RBCs, their volume fraction is still small compared to Ht_t.

At the beginning of a simulation, platelets and RBCs are distributed throughout the tube with random positions and orientations. Any overlap of particles with particles and particles with the tube wall is avoided. The platelets are positioned first, which assures a more homogeneous distribution of them across the tube cross-section. In order to facilitate this procedure, all particles are initially shrunk to half of their linear size and grown afterwards within 4000 time steps. During growth, the particle volume increases with a constant rate and a repulsion force avoids overlap.

The growth process leads to an increase of kinetic energy in the system since there is no fluid dynamics during the growth that could dissipate energy. However, an increase of the kinetic energy would lead to fast motion of the mesh nodes and instability eventu-

ally. A friction force is therefore used to dissipate energy. This force is switched off once the growth process is complete. The exact form of the dissipation force is not significant for this purpose.

After all particles have reached their full size, the simulation starts with a constant fluid density ρ (unity in simulation units) and zero velocity everywhere. The force density $f = p'$ along the tube is switched on instantaneously to drive the flow. Each simulation runs for $N_t = 2 \cdot 10^5$ time steps, i.e. about $208 t_{\mathrm{ad}}$.

4 Simulation results and discussion

The results and discussion are presented in three parts. In section 4.1, the final suspension state is inspected and characterised, and the cell-free layer thickness is investigated. Section 4.2 contains the margination observations and analysis. Platelet dynamics near the tube wall is discussed in section 4.3.

4.1 RBC dynamics and cell-free layer thickness

Fig. 3 shows the final state (after 208 advection times) for the smallest and largest simulated capillary number Ca and each tube diameter D. Both the RBC and platelet configurations depend on the geometry and flow parameters.

At $Ca = 0.1$, RBCs are only weakly deformed, and their dimples are easy to spot. Contrarily, at $Ca = 2.0$, RBCs show a strong and characteristic elongation, and the dimples have disappeared. The CFL is particulary pronounced at higher Ca, and RBCs close to the tube wall tend to align with the wall and form a ring. This leads to a slight increase in the local RBC concentration (Fig. 6(a)) as observed previously (Lei et al, 2013). Furthermore, RBCs in Fig. 3(b) show a typical zigzag configuration that can be found in small blood vessels (McWhirter et al, 2009).

To characterise the deformation of the RBCs, Fig. 4 depicts the average Taylor deformation parameter $D_{\mathrm{T}} = (a-b)/(a+b)$ of all RBCs in the tube. Here, a and b are the two largest semiaxes of the inertia ellipsoid (Krüger et al, 2011), defining the major RBC plane. For an undeformed RBC, $a = b = r_{\mathrm{RBC}}$ and therefore $D_{\mathrm{T}} = 0$. Fig. 4 reveals that D_{T} is strictly increasing with Ca, as expected. The RBC deformation is mostly defined by the ambient viscous stresses and therefore Ca. This is nicely recovered by the collapse of the curves for $D \geq 15\,\mu\mathrm{m}$. For $D = 10\,\mu\mathrm{m}$, however, nearly all RBCs assume a slipper- or parachute-like shape; the Taylor deformation parameter is not a reliabe deformation indicator then.

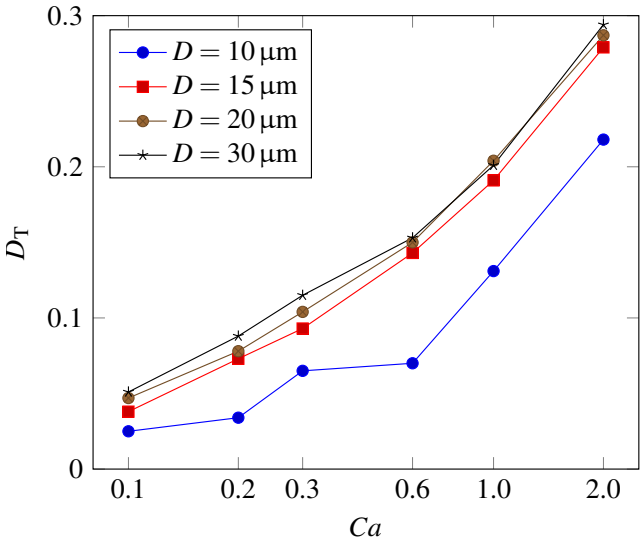

Fig. 4 Average RBC deformation (see main text for the definition of the Taylor deformation parameter D_{T}) as function of capillary number Ca for all investigated tube diameters. Data is time-averaged after the first quarter of the simulation (i.e. between ≈ 50 and 200 advection times). Lines are guides for the eyes.

The rotational state of a flowing RBC is an important observable. For example, we know that RBCs tumble or tank-tread (or perform a more complicated dynamical mode) in simple shear flow. A suitable quantity for describing the rotational activity of an RBC is its average angular velocity $\boldsymbol{\omega}$; it can be obtained by suitably averaging the tangential velocity of all surface elements about the geometrical centre (Krüger et al, 2013). Both tank-treading and tumbling lead to a finite value of $\boldsymbol{\omega}$. The difference is that tank-treading leaves the RBC orientation fixed, while tumbling is a rigid-body rotation. These two modes can be distinguished by investigating the change of the orientation of the RBC's inertia ellipsoid (Krüger et al, 2013). Fig. 5 shows the normalised rotational activity $\boldsymbol{\omega}/\dot{\gamma}_{\mathrm{w}}$ of the RBCs as function of radial position of their centre of mass. Interestingly, the RBCs close to the wall tend to *slide* for $Ca = 0.1$ (nearly no rotational activity) and to tank-tread for $Ca \geq 0.2$ (strong rotational activity). There is no significant change in the rotational activity between $Ca = 0.3$ and $Ca = 2.0$. I did not observe tumbling for those near-wall RBCs; they do not exhibit an appreciable change of their orientation over time (data not shown). This has also been confirmed by visually inspecting the RBC configuration as function of time. The strong wall confinement of those RBCs is probably the reason for them sliding rather than tumbling.

The platelet distribution changes strongly with D and Ca, as discussed in more detail in section 4.2. In summary, platelets prefer to marginate towards the

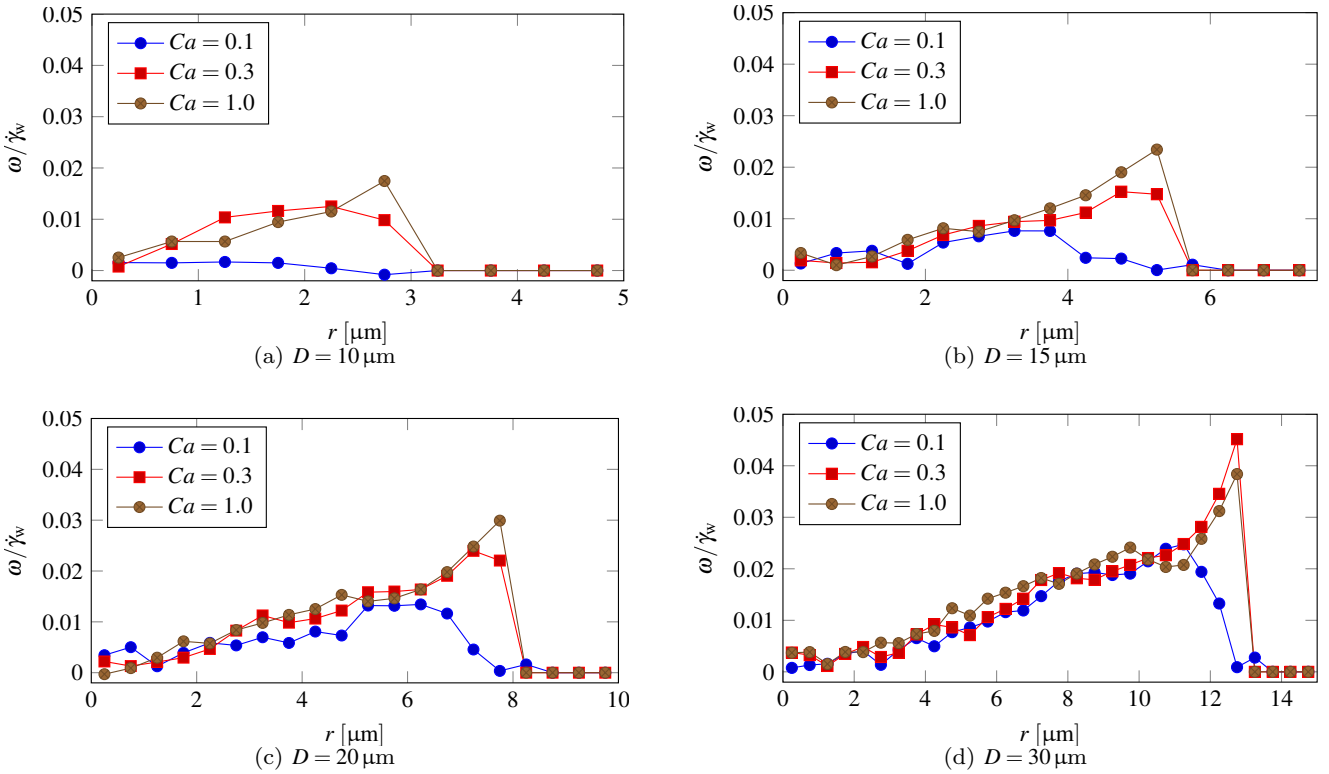

Fig. 5 Average angular velocity ω of the RBCs as function of radial Fig05a of their centre of mass for all investigated tube diameters and selected capillary numbers. Data is time-averaged after the first quarter of the simulation (i.e. between ≈ 50 and 200 advection times), and angular velocities are normalised by $\dot{\gamma}_w$. The magnitude of the temporal fluctuations is comparably to the average. Lines are guides for the eyes.

tube wall with increasing Ca. Also, for smaller D, a larger fraction of platelets resides near the tube wall at the end of the simulations.

There is no unique way to define the CFL thickness ℓ_{CFL} since the edge between the outermost RBCs and the plasma layer is diffuse (Lei et al, 2013). The blurring of the CFL is clearly visible in Fig. 3. In the following, the definition of ℓ_{CFL} is based on the radial tube haematocrit profile $Ht_t(r)$ averaged over time. As shown in Fig. 6(a), $Ht_t(r)$ decreases strongly near the wall. The CFL thickness is defined by the distance from the tube wall where $Ht_t(r)$ reaches $Ht_t/2$.

Fig. 6(b) shows the resulting CFL thickness as function of Ca for different tube diameters D. ℓ_{CFL} is generally increasing with Ca until it saturates above $Ca \approx 0.3$–0.6. This is close to the point where RBC tank-treading replaces tumbling in simple shear flow (Krüger et al, 2013). According to the findings presented earlier in this section, the RBCs next to the tube wall are sliding rather than tumbling at $Ca < 0.2$. The slight decrease of ℓ_{CFL} at $Ca = 2$ is caused by a subtle geometrical rearrangement of the RBCs due to their large deformations. Evidently, the CFL thickness is larger for wider tubes, but the relative thickness ℓ_{CFL}/D is decreasing. In the macroscopic limit, for $D > 100\,\mu m$, the CFL is less important for the effective blood rheology (Lei et al, 2013). Compared to Katanov et al (2015), the CFL thickness values reported here are smaller. This difference is probably caused by varying CFL definitions and different viscosity contrast values; while Katanov et al (2015) used $\Lambda = 1$, it is $\Lambda = 5$ in the present work. According to Katanov et al (2015), a smaller value of Λ results in a larger CFL thickness.

In the following, I use ℓ_{CFL} to identify those platelets that are located between the RBC-rich region and the tube wall.

4.2 Platelet margination

Fig. 7 depicts some example radial platelet positions as function of time. In the following, a platelet is considered being fully marginated when it is located in the CFL vicinity with its radial centre position between $R - 2\ell_{CFL}$ and R (indicated by dotted lines in Fig. 7). As seen in Fig. 6(a), this corresponds to the region between the tube wall and the haematocrit peak at the

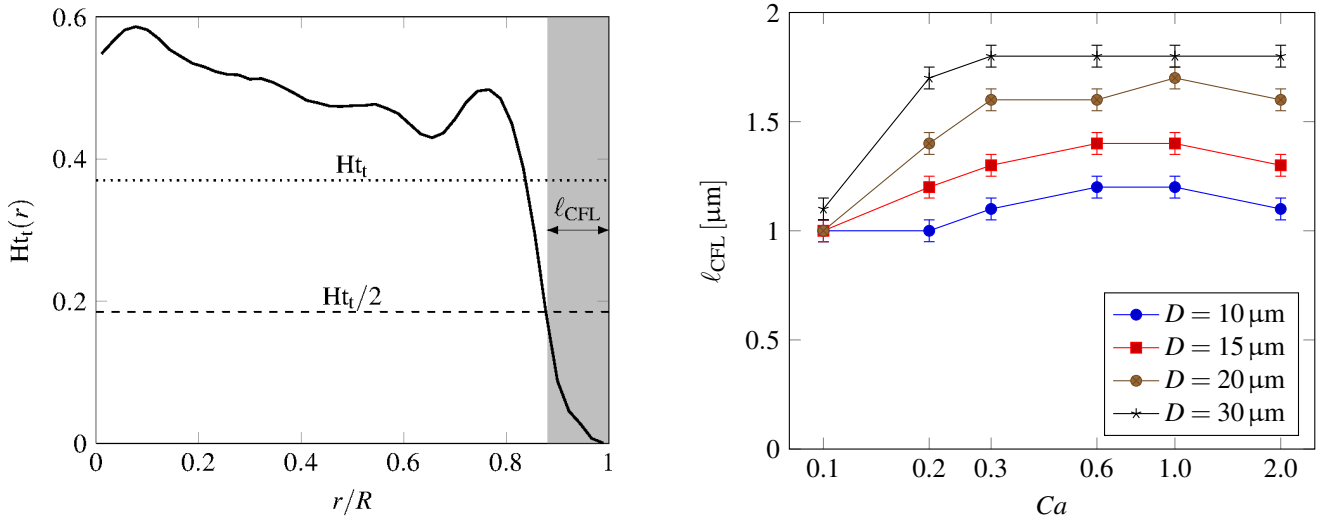

(a) Radial haematocrit distribution ($D = 30\,\mu m$, $Ca = 2.0$)

(b) CFL thickness

Fig. 6 Cell-free layer thickness ℓ_{CFL}. (a) Exemplary radial tube haematocrit profile $Ht_t(r)$ averaged over time. The CFL thickness ℓ_{CFL} (denoted by grey area) is defined as the distance from the wall ($r = R$) to the point where $Ht_t(r)$ reaches half of the average tube haematocrit. (b) ℓ_{CFL} as function of capillary number Ca for all investigated tube diameters D at $Ht_t \approx 37\%$. Error bars are estimates. Lines are guides for the eye. Note that the Ca-axis is logarithmic.

CFL edge. In this region, $Ht_t(r)$ is a strongly decreasing function.

The character of the platelet motion depends on the tube diameter D and the capillary number Ca. Zhao and Shaqfeh (2011) demonstrated previously that platelets show diffusive behaviour in the RBC-rich region until they reach the CFL where they get trapped irreversibly. However, the present data shows that this is only the case for larger capillary numbers ($Ca > 0.2$). Fig. 7 reveals that, for $Ca = 0.1$, several platelets leave the CFL vicinity again. Those platelets do not move far away from the CFL, though; instead they tend to become caught again shortly after. For larger Ca, platelets are trapped in the CFL once they visit it for the first time.

Since it is difficult to extract further information directly from the trajectories in Fig. 7, Fig. 8 shows the time evolution of the average radial platelet position and the fraction of platelets that are located within $2\ell_{CFL}$ from the tube wall. The first observation is that the time for platelets to become trapped increases with tube diameter. In larger tubes, platelets have to move for a longer distance to reach the CFL; this takes more time. From the third and fourth rows in Fig. 8 one can conclude that margination is still ongoing for $D \geq 20\,\mu m$ at the end of the simulation (after 208 advection times). On the contrary, the platelet distributions in the smaller tubes with $D \leq 15\,\mu m$ seem to have reached a quasi-equilibrium.

Secondly, margination and trapping are faster for higher capillary number. However, there is no strong difference between $Ca = 0.3$ and $Ca = 2.0$ as the second and third columns in Fig. 8 show. Zhao and Shaqfeh (2011) observed that the platelet diffusion in the RBC-rich region does not change significantly between $Ca = 1.0$ and $Ca = 2.0$, a fact that is attributed to the saturation of RBC deformation due to the conservation of the RBC surface area. Also Müller et al (2014) reported that the shear-rate dependence of particle margination is most prominent for small shear rates. The strong increase of the margination efficiency between $Ca = 0.1$ and $Ca = 0.3$ in Fig. 8 could be related to the dynamical state of the RBCs. As discussed earlier, RBCs close to the wall slide below and tank-tread above $Ca \approx 0.2$. Reasor Jr et al (2013) hypothesised that tank-treading RBCs may increase the margination efficiency. In fact, for $Ca = 0.1$ (first column in Fig. 8), margination within the first 208 advection times is nearly absent, except for the smallest tube with $D = 10\,\mu m$.

The smallest tube ($D = 10\,\mu m$) plays a special role. Platelets tend to reach the CFL nearly instantaneously, even at $Ca = 0.1$. Therefore, margination in small vessels with $D \leq 10\,\mu m$ seems to be very effective for all capillary numbers. This is in line with the observations by Reasor Jr et al (2013) who reported that, for rigid RBCs, margination only occurs for platelets that are not farther away from the wall than about $5\,\mu m$. Therefore, all platelets in a $10\,\mu m$-tube are always in wall vicinity. This will be further discussed below. Already

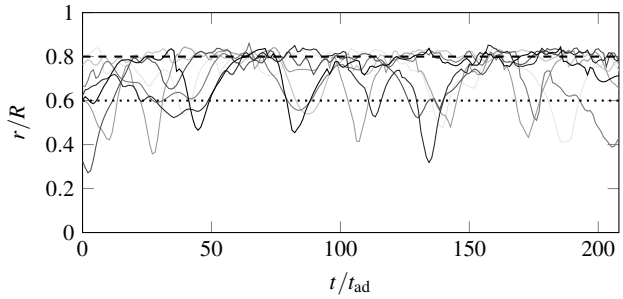

(a) $D = 10\,\mu\text{m}$, $Ca = 0.1$

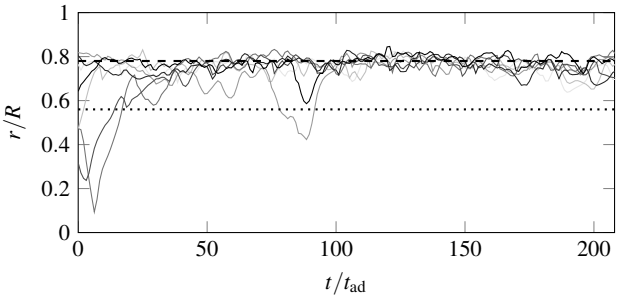

(b) $D = 10\,\mu\text{m}$, $Ca = 2.0$

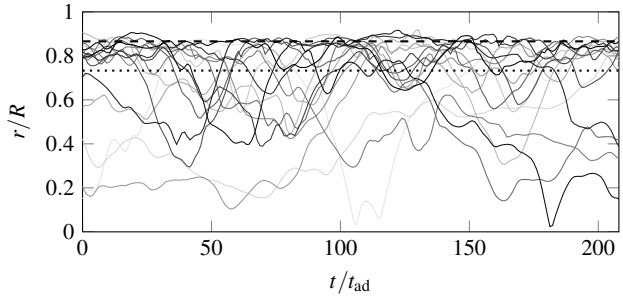

(c) $D = 15\,\mu\text{m}$, $Ca = 0.1$

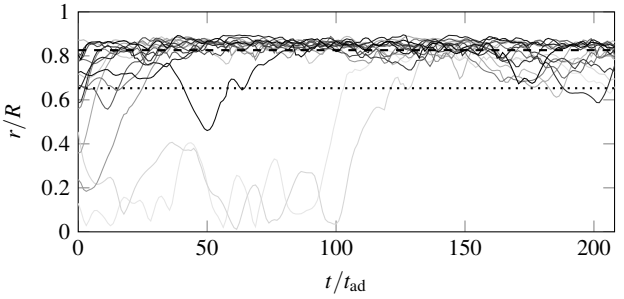

(d) $D = 15\,\mu\text{m}$, $Ca = 2.0$

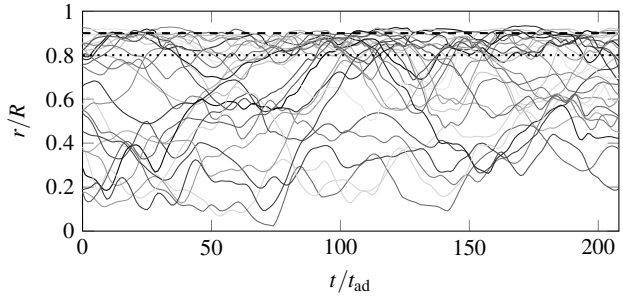

(e) $D = 20\,\mu\text{m}$, $Ca = 0.1$

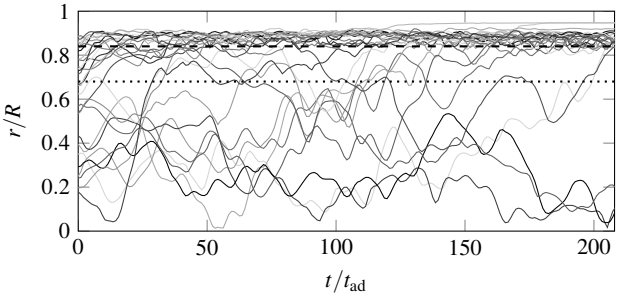

(f) $D = 20\,\mu\text{m}$, $Ca = 2.0$

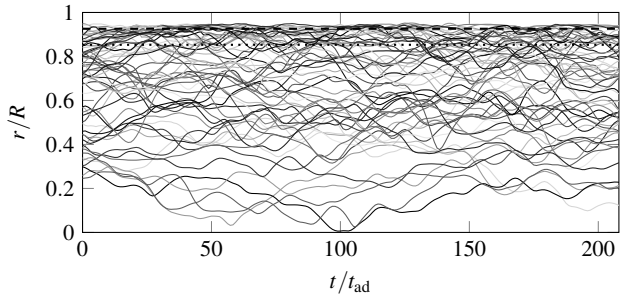

(g) $D = 30\,\mu\text{m}$, $Ca = 0.1$

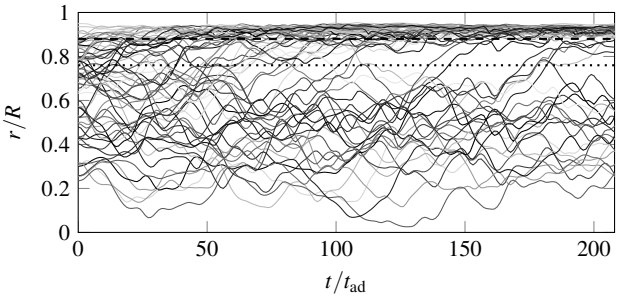

(h) $D = 30\,\mu\text{m}$, $Ca = 2.0$

Fig. 7 Platelet margination for different tube diameters ($D = 10\,\mu\text{m}$ with 7 platelets, $D = 15\,\mu\text{m}$ with 16 platelets, $D = 20\,\mu\text{m}$ with 28 platelets and $D = 30\,\mu\text{m}$ with 63 platelets). The radial position r (normalised by tube radius R) for each platelet is shown for two different capillary numbers ($Ca = 0.1$ and 2.0) as function of dimensionless time. The dashed line denotes the cell-free layer thickness with distance ℓ_{CFL} from the wall. The dotted line denotes twice the CFL thickness, $2\ell_{\text{CFL}}$. Note that platelets are randomly distributed over the pipe cross-section at the start of the simulation. This means that more platelets are initially located at larger radii r since the cross-section area element obeys $\mathrm{d}A = 2\pi r\,\mathrm{d}r$.

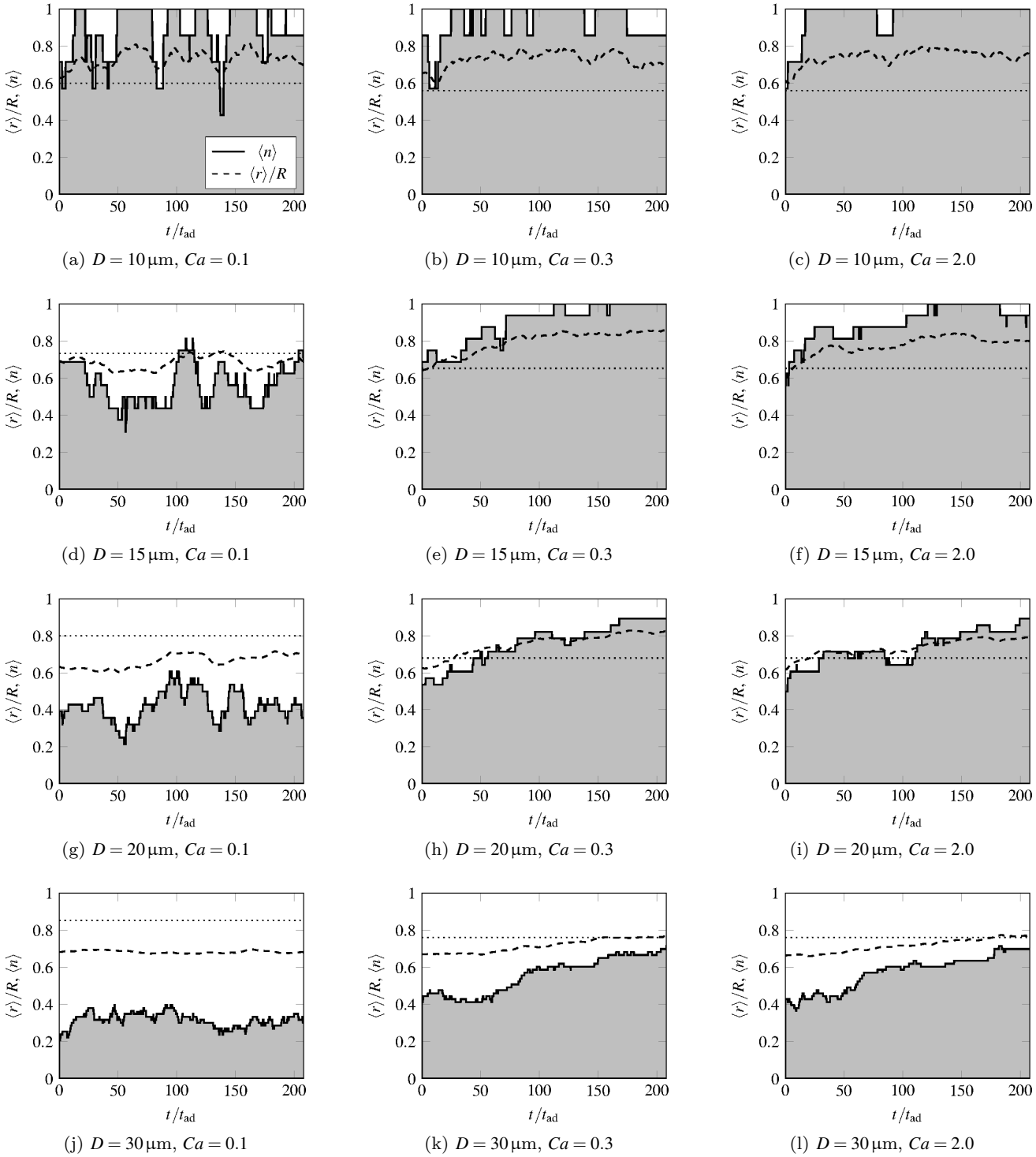

(a) $D = 10\,\mu\text{m}$, $Ca = 0.1$ (b) $D = 10\,\mu\text{m}$, $Ca = 0.3$ (c) $D = 10\,\mu\text{m}$, $Ca = 2.0$

(d) $D = 15\,\mu\text{m}$, $Ca = 0.1$ (e) $D = 15\,\mu\text{m}$, $Ca = 0.3$ (f) $D = 15\,\mu\text{m}$, $Ca = 2.0$

(g) $D = 20\,\mu\text{m}$, $Ca = 0.1$ (h) $D = 20\,\mu\text{m}$, $Ca = 0.3$ (i) $D = 20\,\mu\text{m}$, $Ca = 2.0$

(j) $D = 30\,\mu\text{m}$, $Ca = 0.1$ (k) $D = 30\,\mu\text{m}$, $Ca = 0.3$ (l) $D = 30\,\mu\text{m}$, $Ca = 2.0$

Fig. 8 Average platelet margination for all studied tube diameters D (varied row-wise) and a few capillary numbers ($Ca = 0.1$, 0.3, 2.0, varied column-wise). Dashed lines show the radial position $\langle r \rangle$ averaged over all platelets as function of time. The grey regions bounded by solid lines indicate the number fraction $\langle n \rangle$ of all platelets that are located within a region $2\ell_{\text{CFL}}$ from the tube wall (indicated by horizontal dotted lines).

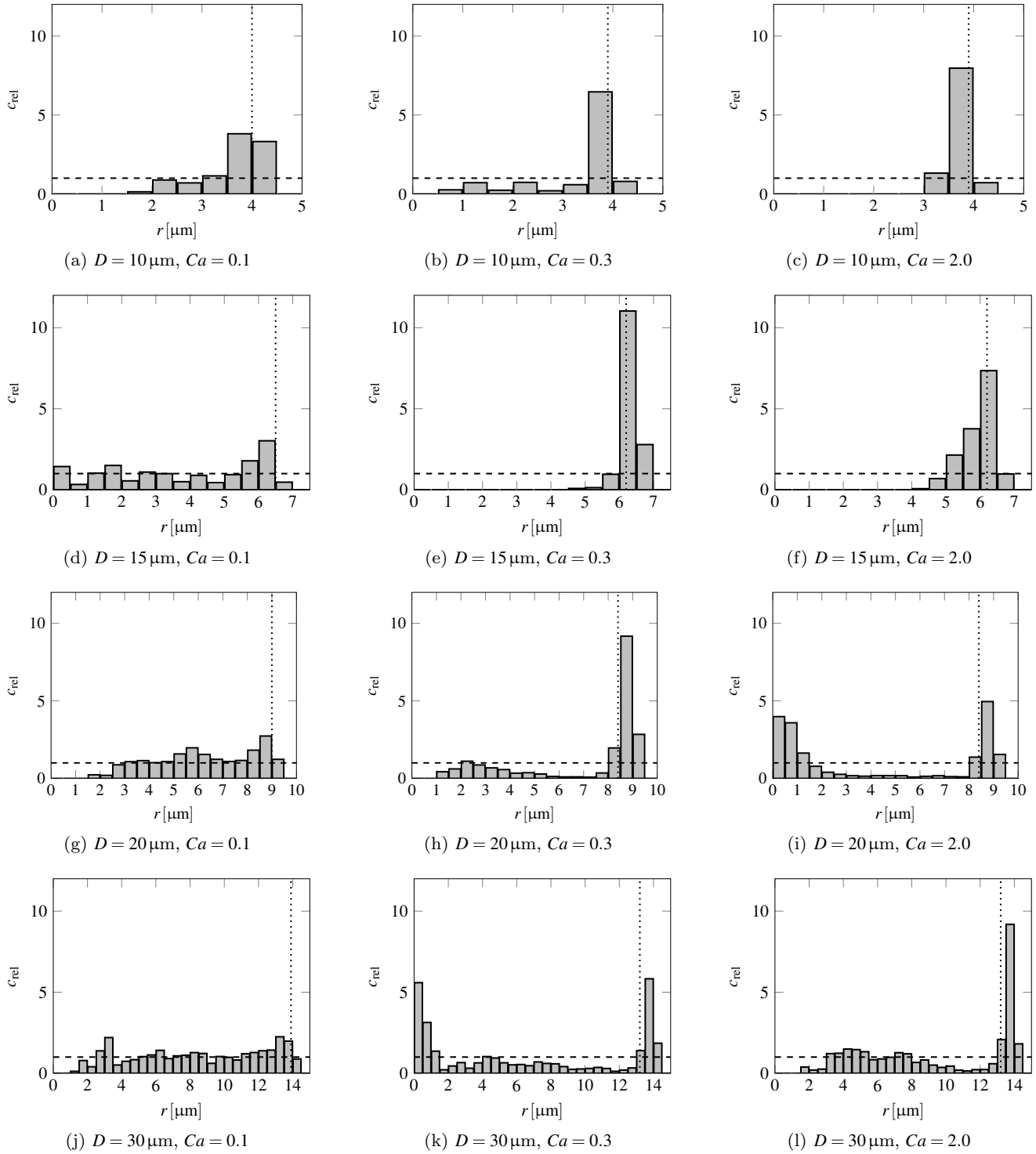

(a) $D = 10\,\mu\mathrm{m}$, $Ca = 0.1$ (b) $D = 10\,\mu\mathrm{m}$, $Ca = 0.3$ (c) $D = 10\,\mu\mathrm{m}$, $Ca = 2.0$

(d) $D = 15\,\mu\mathrm{m}$, $Ca = 0.1$ (e) $D = 15\,\mu\mathrm{m}$, $Ca = 0.3$ (f) $D = 15\,\mu\mathrm{m}$, $Ca = 2.0$

(g) $D = 20\,\mu\mathrm{m}$, $Ca = 0.1$ (h) $D = 20\,\mu\mathrm{m}$, $Ca = 0.3$ (i) $D = 20\,\mu\mathrm{m}$, $Ca = 2.0$

(j) $D = 30\,\mu\mathrm{m}$, $Ca = 0.1$ (k) $D = 30\,\mu\mathrm{m}$, $Ca = 0.3$ (l) $D = 30\,\mu\mathrm{m}$, $Ca = 2.0$

Fig. 9 Radial distribution of relative platelet concentration c_{ref} for different tube diameters D (varying row-wise) and capillary numbers Ca (varying column-wise). The platelet distributions are normalised by the cross-sectional area of each bin such that a homogeneous distribution would lead to a constant line at $c_{\mathrm{rel}} = 1$ (denoted by horizontal dashed line). The bin size is $0.5\,\mu\mathrm{m}$. Data is obtained from platelet centres and averaged between $3N_t/4$ and N_t. The cell-free layer thickness is shown as vertical dotted line.

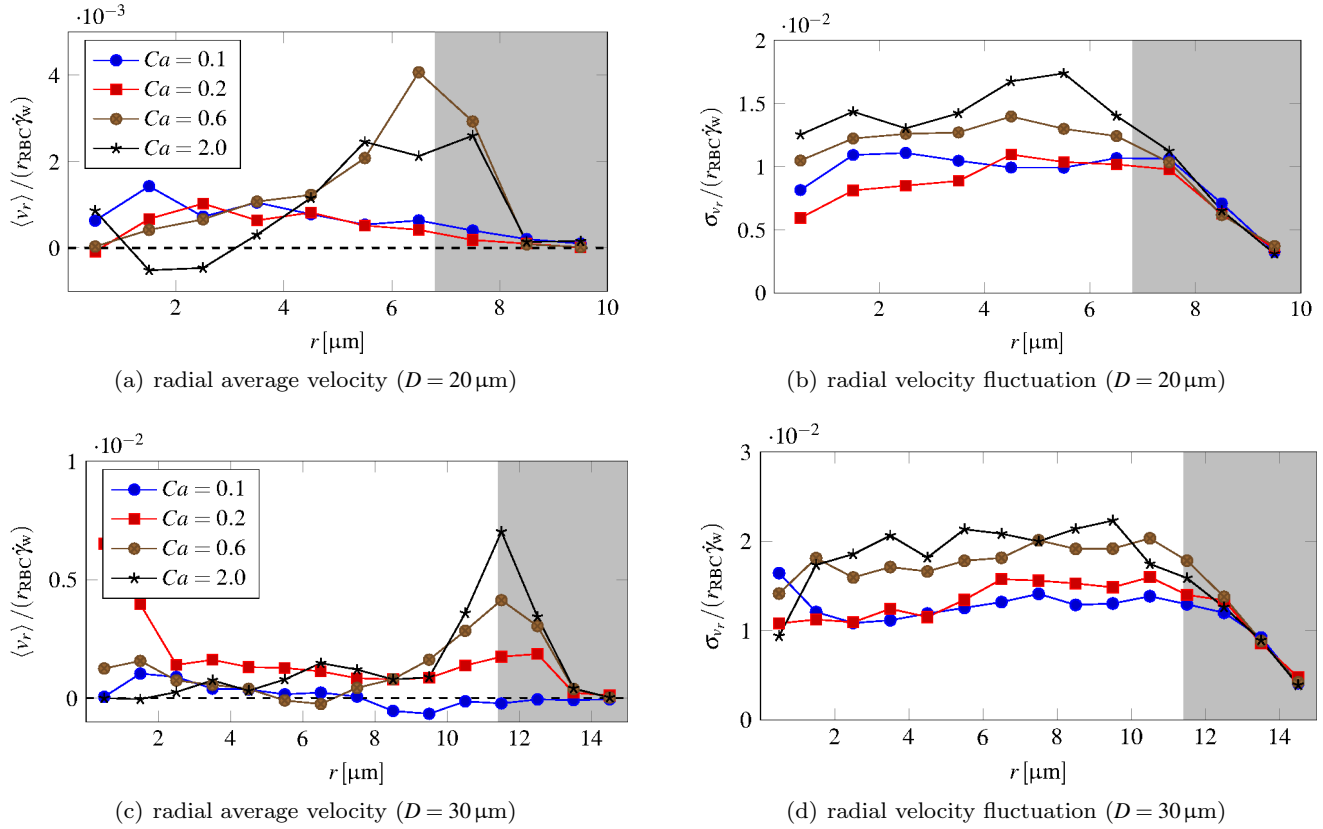

(a) radial average velocity ($D = 20\,\mu\mathrm{m}$)

(b) radial velocity fluctuation ($D = 20\,\mu\mathrm{m}$)

(c) radial average velocity ($D = 30\,\mu\mathrm{m}$)

(d) radial velocity fluctuation ($D = 30\,\mu\mathrm{m}$)

Fig. 10 (a,c) Average radial platelet velocity $\langle v_r \rangle$ and (b,d) its standard deviation σ_{v_r} as function of radial position r. Data is shown for (a,b) $D = 20\,\mu\mathrm{m}$ and (c,d) $D = 30\,\mu\mathrm{m}$. Data is time-averaged after the first quarter of the simulation (i.e. between ≈ 50 and 200 advection times), and velocities are normalised by $r_{\mathrm{RBC}}\dot{\gamma}_{\mathrm{w}}$. The grey-shaded area denotes the CFL vicinity ($2\ell_{\mathrm{CFL}}$). Lines are guides for the eyes.

for a slightly larger tube ($D = 15\,\mu\mathrm{m}$), several platelets remain in the RBC-rich region for an extended period of time if the RBCs are sufficiently rigid ($Ca = 0.1$). For tubes with $D = 20\,\mu\mathrm{m}$ and $30\,\mu\mathrm{m}$, only a fraction of the platelets initially located in the RBC-rich phase diffuse into the CFL during the simulation time. These observations are in line with Müller et al (2014) reporting an increased margination efficiency in smaller vessels.

As a final remark regarding Fig. 8, the number ratio of platelets near the tube wall fluctuates more for smaller Ca. This supports the observation that platelets are not irreversibly trapped in the CFL for $Ca = 0.1$. Further data substantiating this claim will be discussed shortly.

Fig. 9 shows some radial platelet distributions averaged over the final 25% of the simulation time (between ≈ 150 and 200 advection times). These data support the previous interpretations. For $D = 10\,\mu\mathrm{m}$ (first row), margination is very effective, and nearly all platelets are located close to the CFL (vertical dotted line). The situation is different for larger tube diameters with $Ca = 0.1$ (left column). In those cases, there is nearly no margination, and the platelet distribution is close to being homogeneous (horizontal dashed line). For $Ca = 0.3$ and $Ca = 2.0$ (second and third columns in Fig. 9), platelets are effectively transported towards the tube wall.

In Fig. 9(h,i,k,l), a dip in the platelet concentration close to the CFL edge is visible. This suggests that platelets are effectively transported in outward direction when they are close to the CFL edge, therefore decreasing the concentration at $r \approx R - 2\ell_{\mathrm{CFL}}$ and increasing it within the CFL. Platelet diffusion leads to a fresh supply of platelets moving from the RBC-rich region towards the wall until there are no platelets left in the tube interior. Further evidence supporting this interpretation will be discussed below. As mentioned before, this process seems to have completed in Fig. 9(e,f), where the tube radius is relatively small ($D = 15\,\mu\mathrm{m}$). Yet, the process appears to be still ongoing in Fig. 9(h,i,k,l), where the tube is larger. In the latter cases, I expect that all platelets will eventually reach the CFL after a sufficiently long time, but much longer simulations are necessary to decide whether margina-

tion for small Ca is just slow or whether this is already the equilibrium state.

As a remark, there is also a platelet concentration peak near the centreline in Fig. 9(i,k). Note that the absolute number of platelets in that region is small since the bin area decreases linearly with r for $r \to 0$. Therefore, the platelet concentration peak near the CFL edge is caused by many more platelets and is therefore more significant than the peak near $r = 0$. This is nicely borne out in Fig. 3(f) where only three platelets are located near the centreline, but the remaining 25 are close to the CFL. Therefore, the central peak is probably a statistical fluctuation due to the relatively short averaging period and limited platelet number.

To investigate the radial platelet transport in more detail, Fig. 10 shows the average radial platelet velocity $\langle v_r \rangle$ and its standard deviation σ_{v_r} as function of radial position r for $D = 20\,\mu\text{m}$ and $D = 30\,\mu\text{m}$. Due to the small number of platelets and the fast margination, the radial velocity data for $D = 10\,\mu\text{m}$ and $D = 15\,\mu\text{m}$ is too noisy to provide useful information.

The first striking observation from Fig. 10 is that the radial platelet velocity is close to zero everywhere, except near the edge of the CFL (grey area) for $Ca > 0.2$. This shows that platelets are pushed towards the wall if they have reached the edge of the CFL. This effect, however, only exists when RBCs are sufficiently strongly deformed and in the tank-treading state. For the presented tube diameters, collisions between platelets and nearly rigid RBCs ($Ca \leq 0.2$) do not lead to a significant lateral platelet transport near the CFL. Note that the lateral platelet velocity is closely related to the drift term in effective platelet transport models (Eckstein and Belgacem, 1991; Yeh and Eckstein, 1994).

As mentioned earlier, Fig. 8 suggests that the system has not yet reached a steady state. It is crucial to understand that this is a necessity to observe non-zero radial platelet velocities in the first place. In a steady state, there could not be a radial net flux of platelets as this would change the radial concentration profile. Therefore, Fig. 9 and Fig. 10 give important insight into the dynamics *towards* the steady state.

The peak of $\langle v_r \rangle(r)$ coincides with the peak of $Ht_\text{t}(r)$ in Fig. 6(a). Therefore, platelets are already pushed outwards before they have passed the CFL edge. For both tube diameters shown in Fig. 10, $\langle v_r \rangle(r)$ becomes significantly larger than zero when the distance to the wall is about $5\,\mu\text{m}$; this is in good agreement with the results report by Reasor Jr et al (2013).

Fig. 10(b,d) reveals that the radial platelet velocity fluctuation strongly decreases within the CFL. This is an indicator for reduced platelet diffusion in that region.

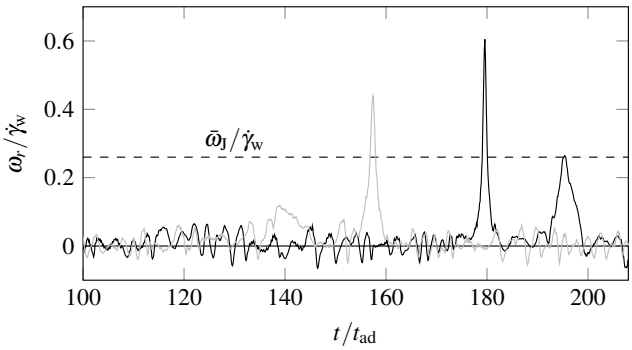

Fig. 11 Angular velocity ω_r normalised by wall shear rate $\dot{\gamma}_\text{w}$ of two platelets (grey and black) near the wall for $D = 20\,\mu\text{m}$ and $Ca = 0.6$. The dashed line indicates the expected average Jeffery frequency $\bar{\omega}_\text{J}$ for an unconfined platelet with aspect ratio 3.6.

One can see that the gradient of σ_{v_r} at the edge of the CFL is larger for higher Ca. This suggests that escaping the CFL becomes increasingly difficult with growing Ca because it is less likely that a platelet is moving fast enough towards the tube axis before it is pushed back. Fig. 10 can therefore explain why more platelets leave the CFL again in Fig. 7 when Ca is small.

Furthermore, the radial velocity fluctuations in Fig. 10 in the RBC-rich region increase with Ca. This may result in a larger platelet diffusivity that further increases the lateral mobility of platelets when Ca is large.

Concluding this section, one can say that non-diffusive platelet margination in tubes with $D \geq 15\,\mu\text{m}$ is only observed when $Ca > 0.2$. This is in good agreement with previous experimental results reporting that margination is only relevant when the wall shear rate is larger than $200\,\text{s}^{-1}$ (Tilles and Eckstein, 1987; Eckstein et al, 1988; Bilsker et al, 1989). According to the definition of Ca in Eq. (9), $Ca = 0.2$ corresponds to $\approx 250\,\text{s}^{-1}$. This threshold value is close to the point where RBCs near the CFL edge start to tank-tread. The onset of tank-treading therefore seems to be necessary for margination. The situation is different for $D = 10\,\mu\text{m}$ where platelets move to the tube wall very fast, even at $Ca = 0.1$. A possible explanation is that many RBCs in Fig. 3(a) fill the entire cross-section of the tube so that platelets can easily slide between them towards the CFL.

4.3 Platelet tumbling and sliding in the cell-free layer

Once platelets are caught in the vicinity of the CFL, they show two main dynamical states: i) tumbling in the local shear flow and ii) sliding parallel to the flow axis (Vahidkhah et al, 2014). The central observable is

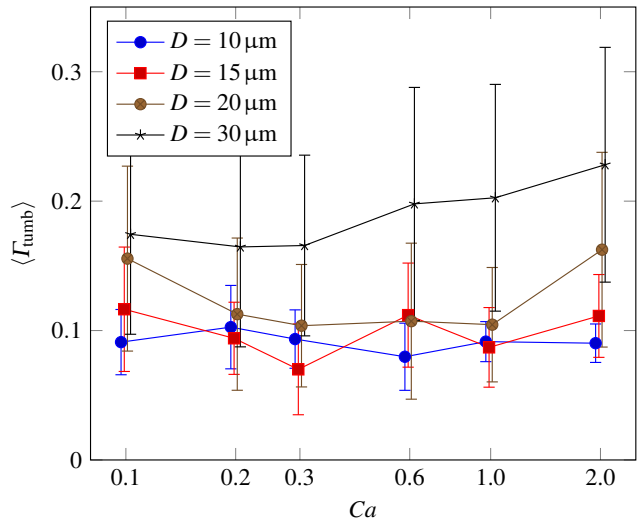

Fig. 12 Normalised tumbling rate Γ_{tumb} averaged over all platelets near the cell-free layer. Error bars indicate ensemble variances. Lines are guides for the eye. Note that the Ca-axis is logarithmic and that symbols are slightly shifted along the Ca-axis to avoid overlap of error bars.

the angular velocity of a platelet in a plane defined by the tube axis and the radial platelet position: ω_r. Fig. 11 shows the time evolution of ω_r for two different platelets in the same simulation near the CFL.

A freely moving platelet with axis aspect ratio p in a shear flow with shear rate $\dot{\gamma}$ would be in a pure tumbling state leading to Jeffery orbits with average angular velocity $\bar{\omega}_{\text{J}}$ (Jeffery, 1922):

$$\frac{\dot{\gamma}}{\bar{\omega}_{\text{J}}} = p + \frac{1}{p}. \tag{11}$$

In the present case, $p = 3.6$, and therefore $\bar{\omega}_{\text{J}} = 0.26\,\dot{\gamma}$ as indicated by the dashed line in Fig. 11. Sliding is caused by confinement due to the presence of the wall on one side of the platelet and the RBCs on the other. Only occasionally a platelet has "enough space" to tumble.

As visible in Fig. 11, tumbling events are defined by localised peaks in ω_r, while sliding is accompanied by low-amplitude fluctuations of ω_r with zero average. Each tumbling event leads to a 180°- or π-rotation of the platelet, called a *flip*. In fact, the time integral of ω_r over one flip turns out to be close to π. A full rotation would therefore require two flips.

An important parameter is the average relative tumbling rate of a platelet in the CFL:

$$\Gamma_{\text{tumb}} = \frac{\bar{\omega}_r}{\bar{\omega}_{\text{J}}} = \frac{1}{\bar{\omega}_{\text{J}}} \frac{\int f(t)\,\omega_r(t)\,\mathrm{d}t}{\int f(t)\,\mathrm{d}t}. \tag{12}$$

To consider only platelets in proximity of the CFL, the function $f(t)$ is defined as

$$f(t) = \begin{cases} 1 & r(t) > R - 2\ell_{\text{CFL}} \\ 0 & \text{otherwise} \end{cases}. \tag{13}$$

Therefore, the integral in the denominator in Eq. (12) is the total time a platelet spends near the CFL: T_{CFL}.

Fig. 12 shows the tumbling rate Γ_{tumb} averaged over all platelets near the CFL. The most striking observation is that tumbling is much less frequent than for a freely moving platelet. The tumbling rate is rather reduced to 10–25% of the value expected for a free platelet, indicating that sliding is the most likely dynamical state in the CFL for the investigated parameters. Also Müller et al (2014) observed a decreased tumbling frequency for ellipsoidal particles trapped in the CFL. Vahidkhah et al (2014) reported that the sliding probability strongly increases with decreasing CFL thickness. Below $\ell_{\text{CFL}} \approx 4\,\mu\text{m}$, which is the case here, sliding starts to occur until it eventually becomes the dominating dynamical mode.

From visual simulation data it follows that platelet flips are correlated with "overtaking" events of individual RBCs that move just at the edge of the CFL. On the one hand, a platelet is dragged along by a passing RBC. On the other hand, platelets find more space in the gaps between RBCs once an RBC has passed. This makes it easier for a platelet to flip, but not all RBC overtaking events lead to a platelet flip.

Interestingly, Γ_{tumb} is rather independent of Ca as seen in Fig. 12. The tube diameter has a stronger effect; larger tubes lead to a higher tumbling rate. This is probably related to an increase of the CFL thickness with D: the thicker the CFL, the smaller the confinement felt by the platelets. Flipping should therefore be easier and more frequent with increasing D but otherwise constant flow parameters (Ht_{t}, Ca).

It is worth mentioning that the errors in Fig. 12, defined by the variance of the ensemble average of all platelets, are relatively large. The reason is that the total number of flips observed is small, and platelets show a wide distribution of number of flips. On average, a platelet flips less than ten times during one simulation.

5 Conclusions

Tube flow of red blood cells (RBCs) and platelets was simulated using a combination of the lattice-Boltzmann, immersed boundary and finite element methods. The aim of this work was to study platelet margination and subsequent platelet dynamics in the cell-free layer (CFL) for different tube diameters D and RBC capillary numbers Ca. Tubes diameters were $D = 10$, 15, 20 and 30 µm, and the investigated capillary numbers range from $Ca = 0.1$, where RBCs are relatively rigid, to $Ca = 2.0$, where RBCs are strongly deformed and elongated. The tube haematocrit is ≈ 37%.

One main result is that platelet margination is facilitated by a non-diffusive radial transport near the CFL edge when $Ca > 0.2$. This is in accordance with previous experimental observations. For smaller Ca, however, margination is less effective, and platelets are not irreversibly trapped in the CFL.

The non-diffusive platelet transport presents itself as a non-zero average platelet velocity in outward direction near the CFL edge. Platelets within the outermost $5\,\mu m$ in the tube are affected by this drift. This explains why platelet margination is very fast for tubes with $D = 10$ and $15\,\mu m$ where essentially all platelets are in wall vicinity. Once a platelet has reached the CFL edge through diffusive motion, it is transported into the CFL due to collisions with tank-treading RBCs. At least for $Ca > 0.2$, I expect this process to continue until no platelets remain in the RBC-rich region.

The simulations also show that the radial platelet velocity fluctuations are strongly suppressed in the CFL. The difference between these fluctuations within the RBC-rich region and the CFL increases with Ca, which explains why platelets are less likely to escape the CFL with increasing Ca.

Furthermore I demonstrated that the predominant dynamical state of platelets in the CFL is sliding rather than tumbling, which is in line with earlier findings. Due to the relatively small CFL thickness at $\approx 37\%$ haematocrit, platelets are strongly confined, and tumbling events are rare. They occur 4–10 times less frequently as expected for an unconfined platelet. The tumbling rate is only a weak function of Ca, but grows with D and therefore the CFL thickness.

The presented results are in accordance with previous experiments and simulations. As such, this work sheds more light on the platelet margination mechanism which is still not well understood. We can see how the explicit modelling of deformable RBCs is necessary to observe margination as an emergent effect. I thus expect this research to stimulate further discussions and contribute to a development of a predictive continuum margination theory.

Acknowledgements I acknowledge the award of a Chancellor's Fellowship from the University of Edinburgh and computer resources at Eindhoven University of Technology. I also thank the three anonymous reviewers for their constructive suggestions that led to an improved manuscript and Gary B. Davies for suggestions to improve the language. There is no conflict of interest. Figures have been created with Ti*k*Z and ParaView.

References

Aarts PA, Bolhuis PA, Sakariassen KS, Heethaar RM, Sixma JJ (1983) Red blood cell size is important for adherence of blood platelets to artery subendothelium. Blood 62(1):214

Aarts PA, Heethaar RM, Sixma JJ (1984) Red blood cell deformability influences platelets–vessel wall interaction in flowing blood. Blood 64(6):1228

Aarts PA, Broek SAvd, Prins GW, Kuiken GDC, Sixma JJ, Heethaar RM (1988) Blood platelets are concentrated near the wall and red blood cells, in the center in flowing blood. Arterioscl Throm Vas 8(6):819–824

Aidun CK, Clausen JR (2010) Lattice-boltzmann method for complex flows. Annu Rev Fluid Mech 42:439–472

AlMomani T, Udaykumar HS, Marshall JS, Chandran KB (2008) Micro-scale Dynamic Simulation of Erythrocyte–Platelet Interaction in Blood Flow. Ann Biomed Eng 36(6):905–920

Bhatnagar PL, Gross EP, Krook M (1954) A model for collision processes in gases. i. small amplitude processes in charged and neutral one-component systems. Phys Rev 94(3):511–525

Bilsker DL, Waters CM, Kippenhan JS, Eckstein EC (1989) A freeze-capture method for the study of platelet-sized particle distributions. Biorheology 26(6):1031

Breugel HFV, Groot PGD, Heethaar RM, Sixma JJ (1992) Role of plasma viscosity in platelet adhesion. Blood 80(4):953

Cadroy Y, Hanson SR (1990) Effects of red blood cell concentration on hemostasis and thrombus formation in a primate model. Blood 75(11):2185

Charrier J, Shrivastava S, Wu R (1989) Free and constrained inflation of elastic membranes in relation to thermoforming - non-axisymmetric problems. J Strain Anal Eng 24(2):55–74

Crowl LM, Fogelson AL (2010) Computational model of whole blood exhibiting lateral platelet motion induced by red blood cells. Int J Numer Meth Biomed Engng 26:471–487

Doddi SK, Bagchi P (2009) Three-dimensional computational modeling of multiple deformable cells flowing in microvessels. Phys Rev E 79(4):046,318

Doggett TA, Girdhar G, Lawshé A, Schmidtke DW, Laurenzi IJ, Diamond SL, Diacovo TG (2002) Selectin-like kinetics and biomechanics promote rapid platelet adhesion in flow: the GPIb [alpha]-vWF tether bond. Biophys J 83(1):194–205

Dupin MM, Halliday I, Care CM, Alboul L, Munn LL (2007) Modeling the flow of dense suspensions of deformable particles in three dimensions. Phys Rev E

75(6):066,707
Eckstein EC, Belgacem F (1991) Model of platelet transport in flowing blood with drift and diffusion terms. Biophys J 60(1):53–69
Eckstein EC, Tilles AW, Millero FJ, et al (1988) Conditions for the occurrence of large near-wall excesses of small particles during blood flow. Microvasc Res 36(1):31–39
Eckstein EC, Koleski JF, Waters CM (1989) Concentration profiles of 1 and 2.5 micrometer beads during blood flow: hematocrit effects. T Am Soc Art Int Org 35:188–190
Eggleton CD, Popel AS (1998) Large deformation of red blood cell ghosts in a simple shear flow. Phys Fluids 10(8):1834–1845
Evans E (1974) Bending Resistance and Chemically Induced Moments in Membrane Bilayers. Biophys J 14(12):923–931
Evans E, Fung YC (1972) Improved measurements of the erythrocyte geometry. Microvasc Res 4(4):335–347
Evans EA, Skalak R (1980) Mechanics and thermodynamics of biomembranes. CRC
Fedosov DA, Pan W, Caswell B, Gompper G, Karniadakis GE (2011) Predicting human blood viscosity in silico. P Natl Acad Sci USA 108(29):11,772–11,777
Fedosov DA, Noguchi H, Gompper G (2014a) Multiscale modeling of blood flow: from single cells to blood rheology. Biomech Model Mechanobiol 13(2):239–258, DOI 10.1007/s10237-013-0497-9
Fedosov DA, Peltomäki M, Gompper G (2014b) Deformation and dynamics of red blood cells in flow through cylindrical microchannels. Soft Matter 10(24):4258–4267
Fogelson AL, Guy RD (2008) Immersed-boundary-type models of intravascular platelet aggregation. Comput Methods Appl Mech Engrg 197(25-28):2087–2104
Fogelson AL, Neeves KB (2015) Fluid Mechanics of Blood Clot Formation. Annu Rev Fluid Mech 47(1):377–403
Freund JB (2014) Numerical Simulation of Flowing Blood Cells. Ann Rev Fluid Mech 46(1):67–95
Frijters S, Krüger T, Harting J (2015) Parallelised Hoshen–Kopelman algorithm for lattice-Boltzmann simulations. Comput Phys Commun 189:92–98
Fåhræus R, Lindqvist T (1931) The viscosity of blood in narrow capillary tubes. Am J Physiol 96:562–568
Goldsmith HL (1971) Red cell motions and wall interactions in tube flow. Fed Proc 30:1578–1588
Goldsmith HL, Mason SG (1967) The microrheology of dispersions. In: Rheology: Theory and Application, Academic Press, vol 4, p 85–250
Goldsmith HL, Turitto VT (1986) Rheological aspects of thrombosis and haemostasis: basic principles and applications. ICTH-Report-Subcommittee on rheology of the international committee on thrombosis and haemostasis. Thromb Haemostasis 55(3):415–435
Gompper G, Schick M (2008) Soft Matter: Lipid Bilayers and Red Blood Cells. Wiley-VCH
Gross M, Krüger T, Varnik F (2014) Rheology of dense suspensions of elastic capsules: normal stresses, yield stress, jamming and confinement effects. Soft Matter 10(24):4360–4372, DOI 10.1039/C4SM00081A
Jeffery GB (1922) The motion of ellipsoidal particles immersed in a viscous fluid. P Roy Soc Lond A Mat 102(715):161–179
Joist JH, Bauman JE, Sutera SP (1998) Platelet adhesion and aggregation in pulsatile shear flow: effects of red blood cells. Thromb Res 92(6):S47–S52
Katanov D, Gompper G, Fedosov DA (2015) Microvascular blood flow resistance: Role of red blood cell migration and dispersion. Microvasc Res 99:57–66, DOI 10.1016/j.mvr.2015.02.006
Krüger T (2011) Computer Simulation Study of Collective Phenomena in Dense Suspensions of Red Blood Cells under Shear. Dissertation, Ruhr University Bochum, Bochum
Krüger T, Varnik F, Raabe D (2011) Efficient and accurate simulations of deformable particles immersed in a fluid using a combined immersed boundary lattice boltzmann finite element method. Comput Math Appl 61:3485–3505
Krüger T, Gross M, Raabe D, Varnik F (2013) Crossover from tumbling to tank-treading-like motion in dense simulated suspensions of red blood cells. Soft Matter 9(37):9008–9015
Krüger T, Holmes D, Coveney PV (2014) Deformability-based red blood cell separation in deterministic lateral displacement devices—A simulation study. Biomicrofluidics 8(5):054,114
Kulkarni S, Dopheide SM, Yap CL, Ravanat C, Freund M, Mangin P, Heel KA, Street A, Harper IS, Lanza F, et al (2000) A revised model of platelet aggregation. J Clin Invest 105(6):783–791
Kumar A, Graham MD (2012a) Margination and segregation in confined flows of blood and other multicomponent suspensions. Soft Matter 8(41):10,536–10,548
Kumar A, Graham MD (2012b) Mechanism of margination in confined flows of blood and other multicomponent suspensions. Phys Rev Lett 109(10):108,102
Ladd AJC (1994) Numerical simulations of particulate suspensions via a discretized boltzmann equation. part 1. theoretical foundation. J Fluid Mech 271:285–309

Lei H, Fedosov DA, Caswell B, Karniadakis GE (2013) Blood flow in small tubes: quantifying the transition to the non-continuum regime. J Fluid Mech 722:214–239

MacMeccan RM, Clausen JR, Neitzel GP, Aidun CK (2009) Simulating deformable particle suspensions using a coupled lattice-Boltzmann and finite-element method. J Fluid Mech 618:13–39

McWhirter JL, Noguchi H, Gompper G (2009) Flow-induced clustering and alignment of vesicles and red blood cells in microcapillaries. P Natl Acad Sci 106(15):6039–6043

Müller K, Fedosov DA, Gompper G (2014) Margination of micro- and nano-particles in blood flow and its effect on drug delivery. Scientific Reports 4

Peerschke EIB, Silver RT, Weksler B, Grigg SE, Savion N, Varon D (2004) Ex vivo evaluation of erythrocytosis-enhanced platelet thrombus formation using the cone and plate (let) analyzer: effect of platelet antagonists. Br J Haematol 127(2):195–203

Peskin CS (1972) Flow patterns around heart valves: A digital computer method for solving the equations of motion. Sue Golding Graduate Division of Medical Sciences, Albert Einstein College of Medicine, Yeshiva University

Peskin CS (2002) The immersed boundary method. Acta Numerica 11:479–517

Qian YH, d'Humières D, Lallemand P (1992) Lattice BGK models for navier-stokes equation. Europhys Lett 17:479–484

Ramanujan S, Pozrikidis C (1998) Deformation of liquid capsules enclosed by elastic membranes in simple shear flow: large deformations and the effect of fluid viscosities. J Fluid Mech 361:117–143

Reasor Jr DA, Mehrabadi M, Ku DN, Aidun CK (2013) Determination of Critical Parameters in Platelet Margination. Ann Biomed Eng 41(2):238–249

Robertson A, Sequeira A, Kameneva M (2007) Hemorheology. In: Hemodynamical Flows, Oberwolfach Seminars, Birkhäuser Basel, p 63–120

Seifert U (1997) Configurations of fluid membranes and vesicles. Adv Phys 46:13–137

Shan X, Chen H (1993) Lattice boltzmann model for simulating flows with multiple phases and components. Phys Rev E 47(3):1815

Shrivastava S, Tang J (1993) Large deformation finite element analysis of non-linear viscoelastic membranes with reference to thermoforming. J Strain Anal Eng 28(1):31–51

Skalak R, Branemark PI (1969) Deformation of Red Blood Cells in Capillaries. Science 164(3880):717–719

Skalak R, Tozeren A, Zarda RP, Chien S (1973) Strain energy function of red blood cell membranes. Biophys J 13(3):245–264

Succi S (2001) The Lattice Boltzmann Equation for Fluid Dynamics and Beyond. Oxford University Press

Sui Y, Chew YT, Roy P, Low HT (2008) A hybrid method to study flow-induced deformation of three-dimensional capsules. J Comput Phys 227(12):6351–6371

Tangelder GJ, Slaaf DW, Teirlinck HC, Alewijnse R, Reneman RS (1982) Localization within a thin optical section of fluorescent blood platelets flowing in a microvessel. Microvasc Res 23(2):214–230

Teirlinck HC, Tangelder GJ, Slaaf DW, Muijtjens AMM, Arts T, Reneman RS (1984) Orientation and diameter distribution of rabbit blood platelets flowing in small arterioles. Biorheology 21(3):317–331

Thompson AJ, Mastria EM, Eniola-Adefeso O (2013) The margination propensity of ellipsoidal micro/nanoparticles to the endothelium in human blood flow. Biomaterials 34(23):5863–5871

Tilles AW, Eckstein EC (1987) The near-wall excess of platelet-sized particles in blood flow: its dependence on hematocrit and wall shear rate. Microvasc Res 33(2):211–223

Turitto VT, Baumgartner HR (1975) Platelet interaction with subendothelium in a perfusion system: physical role of red blood cells. Microvasc Res 9(3):335–344

Turitto VT, Baumgartner HR (1979) Platelet interaction with subendothelium in flowing rabbit blood: Effect of blood shear rate. Microvasc Res 17(1):38–54

Turitto VT, Goldsmith HL (1992) Rheology, transport, and thrombosis in the circulation. Vascular Medicine: A Textbook of Vascular Biology and Diseases Boston, Mass: Little, Brown & Co p 157–204

Turitto VT, Weiss HJ (1980) Red blood cells: their dual role in thrombus formation. Science 207(4430):541–543

Turitto VT, Benis AM, Leonard EF (1972) Platelet diffusion in flowing blood. Ind Eng Chem Fundam 11(2):216–223

Vahidkhah K, Diamond S, Bagchi P (2014) Platelet Dynamics in Three-Dimensional Simulation of Whole Blood. Biophys J 106(11):2529–2540

Waters CM, Eckstein EC (1990) Concentration profiles of platelet-sized latex beads for conditions relevant to hollow-fiber hemodialyzers. Artif Organs 14(1):7–13

Yeh C, Eckstein EC (1994) Transient lateral transport of platelet-sized particles in flowing blood suspensions. Biophys J 66(5):1706–1716

Zhang J, Johnson PC, Popel AS (2007) An immersed boundary lattice boltzmann approach to simulate deformable liquid capsules and its application to micro-

scopic blood flows. Phys Biol 4(4):285–295

Zhao H, Shaqfeh ESG (2011) Shear-induced platelet margination in a microchannel. Phys Rev E 83(6):061,924

Zhao R, Kameneva MV, Antaki JF (2007) Investigation of platelet margination phenomena at elevated shear stress. Biorheology 44(3):161–177